AGU PUBLICATIONS

Geophysical Research Letters

RESEARCH LETTER

10.1002/2014GL059281

Key Points:

- Internal wave (IW) speeds are derived from tandem SAR satellite image pairs
- IW speeds derived from tandem satellites agree well with theoretical model
- IW speed in the South China Sea decreases from southeast to northwest

Correspondence to:
X. Li,
Xiaofeng.Li@noaa.gov

Citation:
Liu, B., H. Yang, Z. Zhao, and X. Li (2014), Internal solitary wave propagation observed by tandem satellites, *Geophys. Res. Lett.*, *41*, 2077–2085, doi:10.1002/2014GL059281.

Received 13 JAN 2014
Accepted 3 MAR 2014
Accepted article online 12 MAR 2014
Published online 25 MAR 2014

Internal solitary wave propagation observed by tandem satellites

Bingqing Liu[1], Hong Yang[1], Zhongxiang Zhao[2], and Xiaofeng Li[3]

[1]College of Marine Sciences, Shanghai Ocean University, Shanghai, China, [2]Applied Physics Laboratory, University of Washington, Seattle, Washington, USA, [3]GST at NOAA/NESDIS, NCWCP E/RA3, College Park, Maryland, USA

Abstract Internal solitary waves (ISWs) are observed 2 times within 30 min in synthetic aperture radar (SAR) image pairs from the Envisat and ERS-2 tandem satellites. Three pairs of SAR images were acquired in the South China Sea (SCS) in April 2007, August 2008, and March 2009, and 13 ISWs were tracked between the image pair in an ArcGIS environment. The phase speeds of these ISWs are calculated from their spatial displacement and time interval. The resultant ISW speeds agree well with the theoretical values estimated from the Sturm-Louisville equation using local bathymetric and monthly climatology ocean stratification data. This technique reveals the spatial variation in the ISWs speed in the water depth between 100 and 4000 m in the SCS. The study shows that ISWs speed is mainly affected by bottom topography and generally decreases from deep to shallow water from east to west and from south to north.

1. Introduction

Internal solitary waves (ISWs) occur ubiquitously in the stratified water of marginal seas and continental shelves [e.g., *Jackson*, 2004; *Alpers et al.*, 2005; *Li et al.*, 2008; *Li et al.*, 2013; *Liu et al.*, 2008; *Zhao et al.*, 2008; *da Silva et al.*, 2012]. ISWs cause large isopycnal displacements and strong local currents in the ocean interior, and their eventual breaking causes intense turbulent mixing [*Liu et al.*, 2004; *Lien et al.*, 2005; *St. Laurent et al.*, 2011]. ISWs play an important role in nutrient distribution, primary productivity, acoustic propagation, coral reef growth, and submarine navigation [e.g., *Wang et al.*, 2007; *Lynch et al.*, 2010; *Lien et al.*, 2012]. It is well known that the ISW-induced currents modulate the sea surface roughness, and therefore, ISWs can be imaged by satellite synthetic aperture radar (SAR) through Bragg backscattering [*Valenzuela*, 1978; *Alpers*, 1985; *Chang et al.*, 2008]. Satellite SAR has long been a principal sensor in the observation of ISWs, because of its all-day, all-weather imaging capability [*Fu and Holt*, 1984; *Liu et al.*, 2008]. In satellite SAR images, one ISW usually appears as a pair of bright and dark stripes, corresponding to the rougher (convergence) and smoother (divergence) surface zones, respectively [*Alpers*, 1985; *Liu et al.*, 1998; *Zheng et al.*, 2001]. ISW parameters, such as geographic location, crest length, and propagation direction, can be directly obtained from SAR images [*Apel et al.*, 1985; *Porter and Thompson*, 1999; *Zheng et al.*, 2001; *Zhao et al.*, 2004].

ISWs may travel over a distance of hundreds of kilometers, due to a balance between nonlinear and dispersive effects [*Apel et al.*, 1985; *Liu et al.*, 1998]. The propagation speed of ISWs is an important dynamic parameter in the study of their generation, evolution, and prediction [*Apel et al.*, 1985; *Jackson*, 2009; *Park and Farmer*, 2013]. The ISW phase speed cannot be accurately determined from one single-satellite SAR image, which only represents a static view of the two-dimensional internal wave field. Assuming the time interval between two neighboring ISW packets is one semidiurnal tidal period (12.42 h), the ISW phase speed can be roughly calculated from the propagation distance between these ISWs [*Porter and Thompson*, 1999; *Li et al.*, 2000; *Liu et al.*, 2004]. Thus, this ISW phase speed is spatially averaged over a distance of a few tens of kilometers.

The ISW phase speed can also be derived from shipboard measurements [e.g., *Orr and Mignerey*, 2003; *Klymak et al.*, 2006] and moored measurements [e.g., *Liu et al.*, 2004; *Xue et al.*, 2013]. For example, *Orr and Mignerey* [2003] reported that their research vessel repeatedly traversed two groups of westward propagating ISWs during ASIAEX 2001, and they obtained the ISW phase speeds by converting the measurements from the ship to Earth coordinates. The method using shipboard measurements is severely limited in space and time by ship time in field experiments. In addition, the uncertainties in the propagation direction of ISWs may lead to considerable errors in estimating their phase speeds. *Orr and Mignerey* [2003] used shipboard radar images to ensure that their research vessel was on a track normal to the ISW crests. The advantage of moored measurements is that moored

Table 1. ERS-2 and Envisat Satellite SAR Image Pairs

Pair	Satellite	Time (UTC)	Center	Spatial Resolution (m)	Swath (km)	Interval (min)	Number of ISWs
C	Envisat	19 Apr 2007 02:02	20°52′N	150	450	29	3
	ERS-2	19 Apr 2007 02:31	115°31′E	30	100		
B	Envisat	16 Aug 2008 14:04	20°43′N	150	450	31	3
	ERS-2	16 Aug 2008 14:35	117°54′E	30	100		
A	Envisat	28 Mar 2009 02:19	20°27′N	150	450	31	7
	ERS-2	28 Mar 2009 02:50	120°06′E	30	100		

long-term measurements can be used to study the temporal variation in the ISW phase speed [*Xue et al.*, 2013]. But their limitations include that (i) the spatial resolution in the resultant ISW phase speed is limited by the spatial distribution of the mooring array and (ii) errors are caused by uncertainties in the propagation direction of ISWs, which also vary with time [*Ramp et al.*, 2010].

Here we report a method for measuring the ISW phase speed using satellite SAR images. In their tandem mission, the European Space Agency (ESA) ERS-2 and Envisat satellites orbited around the Earth approximately along the same orbit, with the Envisat leading the ERS-2 by about 30 min. Thus, one ISW may be observed 2 times by the SAR instruments onboard ERS-2 and Envisat, respectively. In this study, we demonstrate that the propagation speeds of ISWs are obtained for 13 ISWs in three pairs of SAR images. This method is confirmed by comparing with the theoretical phase speeds. One advantage of this method is that it may provide the spatial variation in the ISW phase speed, due to the large coverage of satellite images.

This paper is organized as follows. In section 2, we present the ERS-2 and Envisat SAR images and describe the method for estimating ISW phase speeds from the SAR image pairs. In section 3, the estimation of the ISW phase speed by solving the dynamics equation is presented with climatological ocean stratification and bathymetry. In section 4, the ISW phase speeds derived from SAR image pairs are compared with the theoretical values. Section 5 contains summary and discussions.

2. Data and Method

2.1. Satellite SAR Images

The ERS-2 and Envisat satellites were launched by ESA on 21 April 1995 and 1 March 2002, respectively. These two satellites have a common payload including a SAR and altimeter, and they have similar orbital characteristics. Both satellites orbited around the Earth approximately along the same orbit, with the Envisat leading the ERS-2 by approximately 30 min. We call them tandem satellites. Readers should note that ESA also had two designated ERS-2 and Envisat tandem missions for precise SAR interferometry or interferometric synthetic aperture radar applications. In these tandem missions, the phase information is needed. In this study, only amplitude SAR images are used; therefore, the “tandem” is in a broader sense. Thus, ISWs can be observed 2 times in the ERS-2 and Envisat SAR images approximately 30 min apart.

Three pairs of ERS-2 and Envisat SAR images are analyzed in this study. These SAR images are selected because they cover three different regions in the northeastern South China Sea (SCS). In the SCS, ISWs of amplitude $>$100 m may travel over 500 km in 2 days from Luzon Strait to Dongsha Atoll [*Zhao et al.*, 2004; *Simmons et al.*, 2011; *Farmer et al.*, 2011]. Information about the SAR instruments and images is listed in Table 1. The SAR and advanced SAR (ASAR) instruments are onboard ERS-2 and Envisat, respectively. The ASAR has a swath of approximately 400 km, compared to 100 km of the standard SAR onboard ERS-2. The Envisat and ERS-2 SAR have the pixel spacing of 75 m and 12.5 m, or nominal spatial resolution of 150 m and 25 m, respectively.

All SAR images have been calibrated and georeferenced. Thirteen pairs of ISWs can be detected in these three pairs of SAR images. Their geographic locations are obtained from the SAR images in an ArcGIS environment. The navigational error is about half of a pixel, i.e., 75 m. For a typical ISW wave phase speed of 2 m/s, the ISW propagation distance is about 3.6 km between the 30 min intervals that tandem satellites, ERS-2 and Envisat, images were taken. So, the 75 m navigational error will only affect the ISW phase speed estimation by about 2%.These ISWs are shown in Figure 1, with the ERS-2 and Envisat observations being red and green, respectively. Note that the red curves (ERS-2) always appear to the west of the green

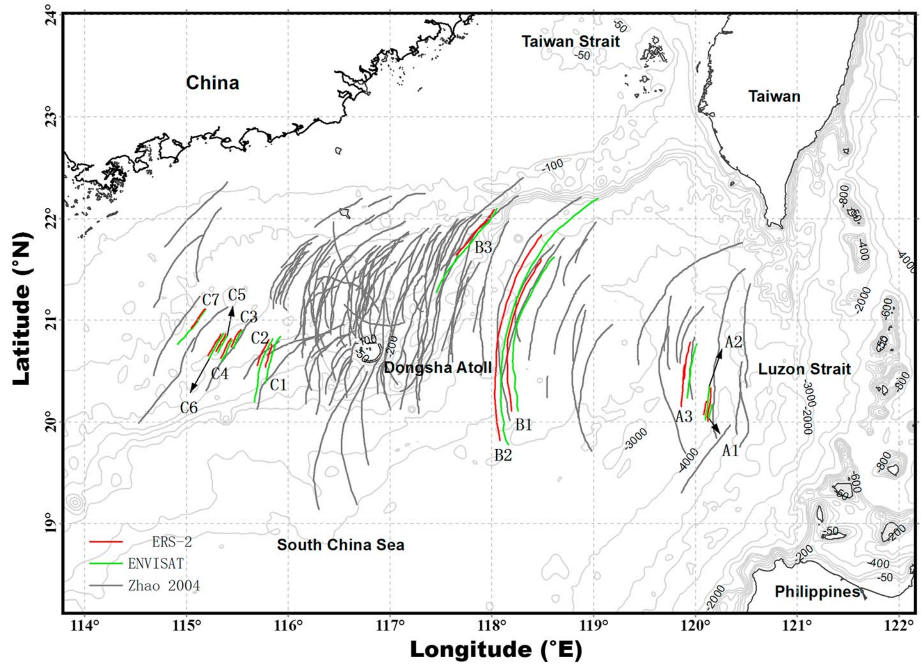

Figure 1. The study area. The black curves are 116 ISWs observed in satellite images (reproduced from *Zhao et al*. [2004]). The Envisat and ERS-2 observed ISWs are shown in green and red, respectively. The red curves (ERS-2) always appear to the west of the green curves (Envisat). The gray contours are bathymetric isobaths. Each curve represents an ISW packet observed in a satellite image.

curves (Envisat), consistent with previous observations that ISWs propagate westward from Luzon Strait to the SCS continental shelf [*Liu et al*., 1998; *Zhao et al*., 2004].

For easy identification, we label the ISWs in these three SAR image pairs alphabetically from east to west: A, B, and C, respectively (Figure 1 and Table 1). ISW packets in each image pair are labeled numerically from east to west, respectively (Figure 1). By this notation, A1 is the easternmost ISW in the SAR image pair acquired on 16 June 2008 (Table 1 and Figure 1). For comparison, 116 ISWs from multiple satellite images collected by *Zhao et al*. [2004] are shown in Figure 1 (black curves). Our new ISW observations generally follow the same pattern in this region observed by *Zhao et al*. [2004].

In each pair of SAR images, one wave packet consists of a leading wave of the largest wavelength followed by trailing wave trains with decreasing wavelength. The leading crest is the longest and brightest. In the deep water, the ISWs are usually in the form of a single wave. The number of waves in a packet increases when the ISW packet propagates onto the shallow shelf. These features are consistent with previous observations of ISWs in the same region [*Zhao et al*., 2004].

The SAR image pair acquired on 28 March 2009 is shown in Figure 2. The bright and dark stripes in the SAR images are interpreted as surface signatures of ISWs. The ISWs generally occur in packets, each of which comprises of a number of ISWs [*Liu et al*., 1998; *Zhao et al*., 2004; *Apel*, 2009]. Two subimages containing ISWs are overlaid in Figure 2c, which reveals the westward propagation of the same ISW packet in a 30 min time span. For a typical wave phase speed of 2 m/s, the propagation distance in 30 min is 3.6 km.

2.2. ISW Phase Speeds Estimated From Tandem Satellite Images

To calculate the propagation speed of ISWs at any position along the wave crests, we draw a bar that is normal to both ISWs, and then measure the distance between the two points where this line interacts with the centers of the two bright stripes (Figure 2c). The measurement errors can be reduced when we average the three measurements with the neighboring points. The distance measurements are executed in ArcGIS software. Typical ISW phase speeds are labeled in Figure 3.

10.1002/2014GL059281

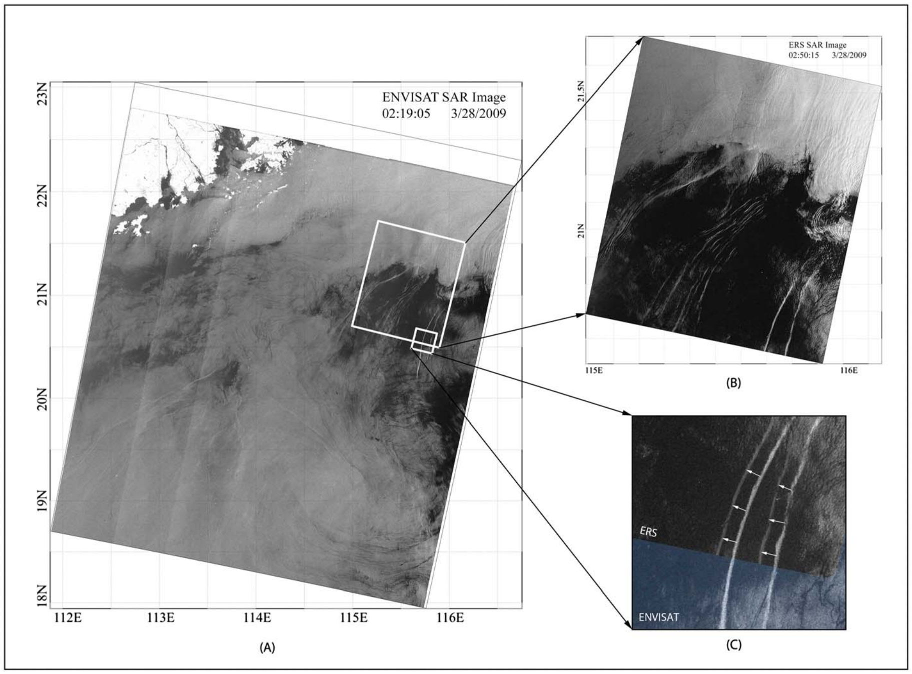

Figure 2. A pair of satellite SAR images acquired within 31 min time interval. (a) An Envisat advanced SAR image acquired at 02:19 UTC 28 March 2009. (b) An ERS-2 SAR image acquired at 02:50 UTC 28 March 2009. (c) The ISW packet was imaged twice by the Envisat and ERS-2 satellites. Their spatial displacements can be measured (labeled as white arrows).

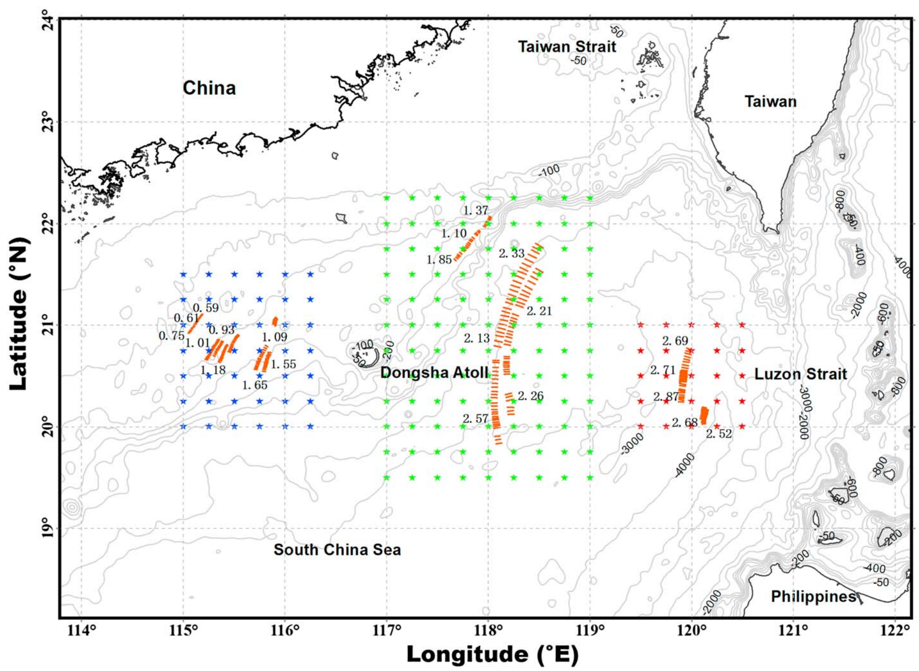

Figure 3. A map showing locations of ISWs observed in three pairs of satellite images. The orange segments are the measured distance that the ISW traveled during the two satellite passes. Blue/red/green color stars represent locations of GDEM climatological ocean stratification data in March/April/August, which corresponds to the three SAR imaging months.

10.1002/2014GL059281

3. Theoretical Phase Speeds From the T-G Equation

The propagation speed of ISWs can be determined theoretically by solving the Taylor-Goldstein (T-G) equation using water depth (H), ocean stratification, and background current information. Under the hydrostatic approximation, the vertical displacement of linear waves $W(z)$ with a background velocity profile $U(z)$ is governed by the T-G equation [*Phillips*, 1977]

$$\left[\frac{\mathrm{d}^2}{\mathrm{d}z^2} - \frac{U_{zz}}{U - C_e} + \frac{N^2(z)}{(U - C_e)^2}\right] W(z) = 0 \tag{1}$$

subjects to the boundary condition

$$W(0) = W(-H) = 0, \tag{2}$$

where $N^2(z)$ is the buoyancy frequency squared, z is the vertical coordinates, U_{zz} is the second-order derivative of $U(z)$, and C_e is the eigenspeed. Note that ISWs are barely affected by the Earth's rotation, because ISWs have frequencies much greater than the local inertial frequency.

Therefore C_e is determined, ordered in importance, by bottom bathymetry, ocean stratification, and background current. Since the time-varying instantaneous background currents are usually small compared to the ISW phase speed, the T-G equation is simplified to the Sturm-Louisville (S-L) equation [*Gill*, 1982]

$$\left(\frac{\mathrm{d}^2}{\mathrm{d}z^2} + \frac{N^2(z)}{C_e^2}\right) \mathrm{W}(z) = 0. \tag{3}$$

The effect of background current is not taken into consideration for the resultant speed C_e from the S-L equation.

Both the water depth and ocean stratification profile are needed to solve equation (3). We obtain local water depth from the 1 min ETOPO1 database [*Amante and Eakins*, 2009] and ocean stratification data from the generalized digital environmental model (GDEM) database [*Teague et al*., 1990]. The GDEM database provides monthly $15' \times 15'$ climatological ocean stratification profiles. The SCS has strong seasonal variation in ocean stratification [*Zhao and Alford*, 2006]. The theoretical ISW phase speed now represents a climatological speed with seasonal variations. In Figure 3, the locations of GDEM ocean stratification data points corresponding to the time (March, April, and August), and the locations of ISWs derived from three SAR image pairs are indicated in blue, red and green stars, respectively.

Long linear internal waves are nondispersive and the eigenspeed is the phase speed of linear internal waves [*Apel et al*., 2009]. Assuming the internal solitary waves are of the Korteweg-deVries type of wave, their nonlinear phase speeds have to be considered. The actual nonlinear ISW phase speed C depends upon its amplitude $C = C_\mathrm{e} + \frac{1}{3}\alpha\eta$, where α is the nonlinear coefficient and η is the wave amplitude. Since the ISW amplitude is unknown, we assume it is 100 m in the deep (depths greater than1000 m) and 20 m in shallow (depths less than1000 m) water [*Orr and Mignerey*, 2003; *Farmer et al*., 2009]. Meanwhile, α is taken as $-0.02\ \mathrm{s}^{-1}$ [*Apel et al*., 1985; *Zhao and Alford*, 2006]. In Figure 4, the obtained theoretical nonlinear ISW phase speeds are shown as blue, red, and green curves for March, April, and August, respectively. As mentioned above, they are the temporally averaged phase speed, with the effects of the temporally varying parameters undetermined.

4. ISW Phase Speeds From SAR and Model

4.1. Spatial Variation of the ISW Phase Speed

The average phase speed of crest line A3 is 2.97 m/s, which is 0.29 m/s faster than the average phase speed of A2 (2.68 m/s). Since the water depth changes very little in this area, this slight discrepancy could be caused by the background currents, in particular, the strong mesoscale eddies [*Ma et al*., 2013; *Park and Farmer*, 2013].

All ISWs in image pair "B" are located between 117°E and 119°E, where the water depth changes abruptly. B1 and B2 are in water depths of 1000–2400 m and B3 is in the 300–450 m range. The average phase speeds of B1, B2, and B3 are 2.16, 2.27, and 1.13 m/s, respectively. The water depth decreases approximately1200 m from south to north along B2, and the corresponding ISW phase speed decreases by about 1.00 m/s.

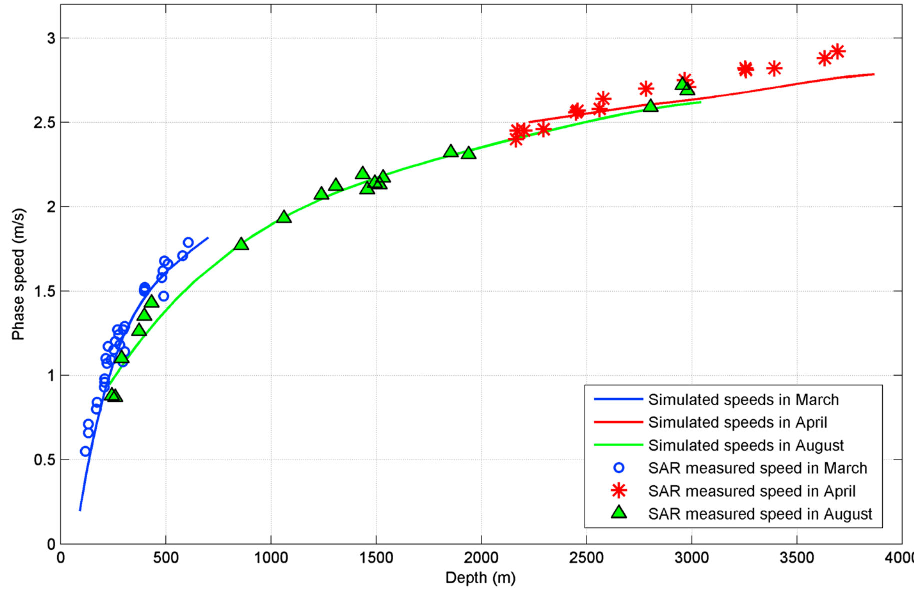

Figure 4. Comparison of phase speed of ISWs from satellite images and theoretical values. The blue/red/green color curves represent the theoretical phase speed derived using GDEM climatological ocean stratification data in March/April/August, respectively. The SAR observed phase speeds in March/April/August are shown as the same color scattered points.

C1 and C2 lie west of the Dongsha Atoll (20°43′N, 116°42′E), which is 330–550 m depth of water. The average phase speed along C2 is 1.61 m/s. The phase speed increases 0.30 m/s with the water depth increasing 100 m. From the C3 to C6 location, the water depth spans from 130 to 400 m. Along C3 to C6, the average phase speed increases 0.16 m/s from east to west with the relevant water depth increasing by about 150 m. All ISWs from C3 to C6 show a distinct signature that the phase speed undergoes an increase from south to north, and the phase speed is about 1.29 m/s at the deepest location compared to the average phase speed of 1.10 m/s. The packets still continue to propagate westward to shallow water, and the average phase speed of C7 is 0.66 m/s in 100–200 m of water depth.

Figure 3 shows 13 ISWs from satellite SAR images overlaid with bathymetric contours. It shows that the phase speed of ISWs decrease gradually with water depth. Stratification also affects the propagation of ISW. Later in a model simulation, we shall show that this parameter has less effect on the ISW propagation than the bathymetry.

4.2. Comparisons With Theoretical Values

The ISW phase speeds derived from SAR and the S-L equation using the corresponding monthly ocean stratification data are plotted versus water depth in Figure 4. Symbols in different colors represent the ISW phase speeds extracted from three SAR image pairs acquired in three different months. The colors are consistent with the ocean stratification profile location symbols in Figure 3. The theoretical phase speeds from the S-L equation are shown as the blue/red/green curve for March/April/August, respectively. The curves are smoothed with a three-point moving average. One can see that the theoretical speeds calculated from climatological stratification and bathymetry generally agree well with the results from the SAR image pairs. The ISW phase speeds are closely related to water depth. At the deep water location of 3725 m, the ISW phase speed is 2.72 m/s, compared to 0.09 m/s at the shallowest water.

The average phase speed extracted from SAR pairs at 100–240, 240–350, and 350–550 m water depth are about 0.66, 1.00, and 1.60 m/s, respectively. It increases to 2.10 m/s at 1000–2000 m depth and 2.70 m/s at 2500–3500 m depth. The averaged theoretical phase speed of ISWs in 100–240, 240–350, and 350–550 m water depth are 0.70, 1.17, and 1.49 m/s, respectively. The phase speed of ISW in the SCS decreases with the shoaling bottom from east to west. Both are proved by tandem satellite SAR pairs and T-G simulation. Taking the westernmost packets as an example, we find that the ISW phase decreases from 1.71 m/s in C2 to 0.54 m/s in C7.

We also show that using interpacket distance to estimate ISW phase speed may have a large error. Taking the westernmost packets as an example, the separation distance between two neighboring ISW packets C6 and C7 is 29.4 km, which is smaller than the 46.5 km between the neighboring C2 and C6. This shows that assuming the ISW packets are separated by semidiurnal tide of 12.42 h is not an accurate enough assumption to study the variation of ISW propagation. However, the decreasing of packet-to-packet distance indicates that the propagation speed of ISWs decreases as they propagate westward. All wave crests in C3–C6 show a distinct signature that the phase speed undergoes a decrease from south to north; the phase speed is about 1.29 m/s at the deepest location and the averaged phase speed is 1.10 m/s. The phase speeds of each packet decrease gradually from south to north and from east to west in the northeast SCS.

The SAR-derived phase speeds are directly measured from the spatial displacements. It measures effects of background current, although small compared to the ISW phase speed, and instantaneous ocean stratification. However, the S-L solution is the only climatological solution. Due to the lack of simultaneous field measurements, the phase speed variation caused by background currents is not taken into consideration. This does not affect our comparison with SAR observations, as the background current was an order of a magnitude smaller than the ISW phase speed.

In Figure 4, in the range of 250–750 m depth, one can observe the difference of ISW phase speeds using SAR estimation and model simulation in different seasons, March is represented as blue and August as green. The ISW propagates faster in March than that in August due to the deeper mixed layer. However, this difference is not very significant; it is on the order of 10% at the depth of 500 m. In the deep water between 2200 and 3200 m, the ISW phase speed theoretical curves for August (green) and April (red) have no apparent difference, indicating that the ocean stratification is not as important as water depth for determining the ISW phase speed.

5. Summary and Discussions

SAR image pairs are acquired from the tandem satellites ERS-2 and Envisat. The ERS-2 and Envisat orbited around the Earth along approximately the same orbit, with the Envisat leading the ERS-2 by 30 min. Therefore, ISWs can be observed 2 times within 30 min in the SAR image pairs which provides more information on the propagation of ISWs. We have demonstrated that the ISW speed can be accurately determined from SAR image pairs, using 13 ISWs observed in three pairs of SAR images in the SCS. After applying image geolocation information, we can extract the locations of the ISWs in an ArcGIS environment. The spatial displacements are measured, and thus, the ISW phase speeds are calculated. In particular, the ISW phase speed can be obtained at different locations along the wave crest of an ISW, thus yielding the spatial variation of the ISW phase speed.

The ISW phase speeds estimated by this technique agree very well with the theoretical values from the S-L equation plus the nonlinear phase speed. Despite uncertainties and limitations, the comparison of ISW phase speeds from SAR images and from the S-L equation provides sufficient evidence that the ISW phase speeds retrieved from satellite SAR image pairs are accurate.

The ISW phase speed is mainly dependent on water depth. In the northeastern SCS, the ISW phase speed generally decreases from east to west and from south to north. It explains the ISW refraction while they propagate onto the SCS continental shelf. The ISW phase speed in the northeastern SCS is complex and exhibits strong spatial variability, determined by many factors. There is strong seasonal variation in the ISW phase speed. In the future, more satellite images are necessary to investigate this phenomenon. Additionally, the background current is a contributing factor, as shown in the T-G equation. Recent studies using field measurements have observed the effects of the Kuroshio and eddy on the ISW phase speed [*Ma et al*., 2013; *Park and Farmer*, 2013]. The ISW phase speed from SAR image pairs contains instantaneous information. Therefore, the results can be used to investigate the Kuroshio's effects.

We have focused on the northeastern SCS, where ISWs have received much attention due to their impressive scales and regular occurrence. This method might be applied to study ISW propagation in other hot spot regions such as the New Jersey coast [*Xue et al*., 2012], the Portugal coast [*da Silva et al*., 2007], Mozambique Channel [*da Silva et al*., 2009], the Red Sea [*da Silva et al*., 2012], and the Iberian shelf [*da Silva et al*., 2007; *Magalhães and da Silva*, 2012].

This technique can be expanded to remote sensing images from other satellite sensors, such as MODIS (Moderate Resolution Imaging Spectroradiometer) images from Terra and Aqua, and VIIRS (Visible Infrared Imaging Radiometer Suite) images from NPOESS Preparatory Project (NPP) (National Polar-orbiting Operational Environmental Satellite System Preparatory Project). The SAR, MODIS, and VIIRS images can be combined to estimate the phase speed of ISWs. An advantage of this method is that these satellites have large swath of over 2000 km, and thus, the spatial variation of ISW phase speed can be evaluated, while other field measurements using ship and moorings do not have such simultaneous large coverage. The disadvantage is that the optical images are severely contaminated by clouds. Synergy of SAR and optical images is ideal for tracking ISW in the SCS in the near future when ESA's Sentinel-1 SAR images become freely and openly available.

Acknowledgments

The Envisat and ERS SAR images were provided by the European Space Agency under Envisat Projects 19011 and 6133. This work was supported by Shanghai Dongfang Scholar Program. The views, opinions, and findings contained in this report are those of the authors and should not be construed as an official NOAA or U.S. government position, policy, or decision.

The Editor thanks two anonymous reviewers for their assistance in evaluating this paper.

References

Alpers, W. (1985), Theory of radar imaging of internal waves, *Nature*, *314*, 245–247.

Alpers, W., M.-X. He, K. Zeng, L.-F. Guo, and X.-M. Li (2005), The distribution of internal waves in the East China Sea and the Yellow Sea studied by multi-sensor satellite images, In *Proceedings of the 2005 International Geoscience and Remote Sensing Symposium* (*IGARSS'05*), Seoul, Korea.

Amante, C., and B. W. Eakins (2009), ETOPO1 1 arc-minute global relief model: Procedures, data sources and analysis, NOAA Technical Memorandum NESDIS NGDC-24, 19 pp.

Apel, J. R. (2009), Oceanic internal waves and solitons, in *Synthetic Aperture Radar Marine User's Manual*, edited by C. R. Jackson and J. R. Apel, pp. 189–206, NOAA, Washington, D. C.

Apel, J. R., J. R. Holbrook, A. K. Liu, and J. J. Tsai (1985), The Sulu Sea internal soliton experiment, *J. Phys. Oceanogr.*, *15*, 1625–1651.

Chang, M.-H., R.-C. Lien, Y. J. Yang, T. Y. Tang, and J. Wang (2008), A composite view of surface signatures and interior properties of nonlinear internal waves: Observations and applications, *J. Atmos. Oceanic Technol.*, *25*, 1218–1227, doi:10.1175/2007JTECHO574.1.

da Silva, J. C. B., A. L. New, and A. Azevedo (2007), On the role of SAR for observing "local generation" of internal solitary waves off the Iberian Peninsula, *Can. J. Remote Sens.*, *33*(5), 388–403, doi:10.5589/m07-041.

da Silva, J. C. B., A. L. New, and J. M. Magalhães (2009), Internal solitary waves in the Mozambique Channel: Observations and interpretation, *J. Geophys. Res.*, *114*, C05001, doi:10.1029/2008JC005125.

da Silva, J. C. B., J. M. Magalhães, T. Gerkema, and L. R. M. Maas (2012), Internal solitary waves in the Red Sea: An unfolding mystery, *Oceanography*, *25*, 96–107, doi:10.5670/oceanog.2012.45.

Farmer, D. M., M. H. Alford, R.-C. Lien, Y. J. Yang, M.-H. Chang, and Q. Li (2011), From Luzon Strait to Dongsha Plateau: Stages in the life of an internal wave, *Oceanography*, *24*(4), 64–77, doi:10.5670/oceanog.2011.95.

Farmer, D., Q. Li, and J.-H. Park (2009), Internal wave observations in the South China Sea: The role of rotation and non-linearity, *Atmos. Ocean*, *47*(4), 267–280, doi:10.3137/OC313.2009.

Fu, L.-L., and B. Holt (1984), Internal waves in the Gulf of California: Observations from a spaceborne radar, *J. Geophys. Res.*, *89*(C2), 2053–2060.

Gill, A. E. (1982), *Atmosphere–Ocean Dynamics*, 662, Academic Press, San Diego, Calif.

Jackson, C. R. (2004), *An Atlas of Internal Solitary-Like Waves and Their Properties*, 2nd ed., Global Ocean Associates, Washington, D. C. [Available at http://www.internalwaveatlas.com/Atlas2index.html.]

Jackson, C. R. (2009), An empirical model for estimating the geographic location of nonlinear internal solitary waves, *J. Atmos. Oceanic Technol.*, *26*, 2243–2255.

Klymak, J. M., R. Pinkel, C.-T. Liu, A. K. Liu, and L. David (2006), Prototypical solitons in the South China Sea, *J. Geophys. Res.*, *33*, L11607, doi:10.1029/2006GL025932.

Li, X., P. Clemente-Colon, and K. Friedman (2000), Estimating oceanic mixed layer depth from internal wave evolution observed from RADARSAT-1 SAR, *Johns Hopkins Univ. APL Tech. Digest*, *21*(1), 130–135.

Li, X., Z. Zhao, and W. G. Pichel (2008), Internal solitary waves in the northwestern South China Sea inferred from satellite images, *Geophys. Res. Lett.*, *35*, L13605, doi:10.1029/2008GL034272.

Li, X., C. R. Jackson, and W. G. Pichel (2013), Internal solitary wave refraction at Dongsha Atoll South China Sea, *Geophys. Res. Lett.*, *40*, 3128–3132, doi:10.1002/grl.50614.

Lien, R.-C., T. Y. Tang, M.-H. Chang, and E. A. D'Asaro (2005), Energy of nonlinear internal waves in the South China Sea, *Geophys. Res. Lett*, *32*, L05615, doi:10.1029/2004GL022012.

Lien, R.-C., E. A. D'Asaro, F. S. Henyey, M.-H. Chang, T. Y. Tang, and Y.-J. Yang (2012), Trapped core formation within a shoaling nonlinear internal wave, *J. Phys. Oceanogr.*, *42*, 511–525, doi:10.1175/2011JPO4578.1.

Liu, A. K., S. Y. Chang, M.-K. Hsu, and N. K. Liang (1998), Evolution of nonlinear internal waves in East and South China Seas, *J. Geophys. Res.*, *103*, 7995–8008.

Liu, A. K., S. R. Ramp, Y. Zhao, and T. Y. Tang (2004), A case study of internal solitary wave propagation during ASIAEX 2001, *IEEE J. Ocean. Eng.*, *29*(4), 1144–1156.

Liu, A. K., C.-R. Ho, and C.-T. Liu (2008), *Satellite Remote Sensing of South China Sea*, 312, Tingmao Publishing Co., Taipei.

Lynch, J. F., Y.-T. Lin, T. F. Duda, and A. E. Newhall (2010), Acoustic ducting, reflection, refraction, and dispersion by curved nonlinear internal waves in shallow water, *IEEE J. Ocean. Eng.*, *35*, 12–27.

Ma, B. B., R.-C. Lien, and D. S. Ko (2013), The variability of internal tides in the northern South China Sea, *J. Oceanogr.*, *69*, 619–630, doi:10.1007/s10872-013-0198-0.

Magalhães, J. M., and J. C. B. da Silva (2012), SAR observations of internal solitary waves generated at the Estremadura Promontory off the west Iberian coast, *Deep-Sea Res. Part I- Oceanogr. Res. Pap.*, *69*, 12–24, doi:10.1016/j.dsr.2012.06.002.

Orr, M. H., and P. C. Mignerey (2003), Nonlinear internal waves in the South China Sea: Observation of the conversion of depression internal waves to elevation internal waves, *J. Geophys. Res.*, *108*(C3), 3064, doi:10.1029/2001JC001163.

Park, J.-H., and D. Farmer (2013), Effects of Kuroshio intrusions on nonlinear internal waves in the South China Sea during winter, *J. Geophys. Res. Oceans*, *118*, 7081–7094, doi:10.1002/2013JC008983.

Phillips, O. M. (1977), *The Dynamics of the Upper Ocean*, 2nd ed., 336 pp., Cambridge Univ. Press, London, U. K.

Porter, D. J., and D. R. Thompson (1999), Continental shelf parameters inferred from SAR internal wave observations, *J. Atmos. Oceanic Technol.*, *16*, 475–487.

Ramp, S. R., Y. J. Yang, and F. L. Bahr (2010), Characterizing the nonlinear internal wave climate in the northeastern South China Sea, *Nonlinear. Proc. Geophys.*, *17*(5), 481–498, doi:10.5194/npg-17-481-2010.

Simmons, H., M.-H. Chang, Y.-T. Chang, S.-Y. Chao, O. Fringer, C. R. Jackson, and D. S. Ko (2011), Modeling and prediction of internal waves in the South China Sea, *Oceanography*, *24*(4), 88–99, doi:10.5670/oceanog.2011.97.

St. Laurent, L., H. Simmons, T. Y. Tang, and Y. H. Wang (2011), Turbulent properties of internal waves in the South China Sea, *Oceanography*, *24*(4), 78–87, doi:10.5670/oceanog.2011.96.

Teague, W. J., M. J. Carron, and P. J. Hogan (1990), A comparison between the Generalized Digital Environmental Model and Levitus climatologies, *J. Geophys. Res.*, *95*, 7176–7183.

Valenzuela, R. G. (1978), Theories for the interaction of electromagnetic and ocean waves—A review, *Boundary Layer Meteorol.*, *13*, 61–85.

Wang, Y.-H., C.-F. Dai, and Y.-Y. Chen (2007), Physical and ecological processes of internal waves on an isolated reef ecosystem in the South China Sea, *Geophys. Res. Lett.*, *34*, L18609, doi:10.1029/2007GL030658.

Xue, J., H. C. Graber, B. Lund, and R. Romeiser (2013), Amplitudes estimation of large internal solitary waves in the Mid-Atlantic Bight using synthetic aperture radar and marine X-band radar images, *IEEE Trans. Geosci. Remote Sens.*, *51*(6), 3250–3258.

Zhao, Y., A. K. Liu, and M.-K. Hsu (2008), Internal wave refraction observed from sequential satellite images, *Int. J. Remote Sens.*, *29*(21), 6381–6390.

Zhao, Z., and M. H. Alford (2006), Source and propagation of internal solitary waves in the northeastern South China Sea, *J. Geophys. Res.*, *111*, C11012, doi:10.1029/2006JC003644.

Zhao, Z., V. Klemas, Q. Zheng, and X.-H. Yan (2004), Remote sensing evidence for baroclinic tide origin of internal solitary waves in the northeastern South China Sea, *Geophys. Res. Lett.*, *31*, L06302, doi:10.1029/203GL019077.

Zheng, Q., Y. Yuan, V. Klemas, and X.-H. Yan (2001), Theoretical expression for an oceanic internal soliton synthetic aperture radar image and determination of the soliton characteristic half width, *J. Geophys. Res.*, *106*, 31,415–31,423.